


Topological surface states of MnBi_2Te_4 at finite temperatures and at domain walls

Kevin F. Garrity¹,^{*} Sugata Chowdhury, and Francesca M. Tavazza

Material Measurement Laboratory, National Institute of Standards and Technology, Gaithersburg, Maryland 20899, USA

 (Received 6 March 2020; revised 17 November 2020; accepted 24 November 2020; published 24 February 2021)

MnBi_2Te_4 has recently been the subject of intensive study, due to the prediction of axion insulator, Weyl semimetal, and quantum anomalous Hall insulator phases, depending on the structure and magnetic ordering. Experimental results have confirmed some aspects of this picture, but several experiments have seen zero-gap surface states at low temperature, in conflict with expectations. In this work, we develop a first-principles-based tight-binding model that allows for arbitrary control of the local spin direction and spin-orbit coupling, enabling us to accurately treat large unit-cells. Using this model, we examine the behavior of the topological surface state as a function of temperature, finding a gap closure only above the Néel temperature. In addition, we examine the effect of magnetic domains on the electronic structure, and we find that the domain wall zero-gap states extend over many unit-cells. These domain wall states can appear similar to the high-temperature topological surface state when many domain sizes are averaged, potentially reconciling theoretical results with experiments.

DOI: [10.1103/PhysRevMaterials.5.024207](https://doi.org/10.1103/PhysRevMaterials.5.024207)

I. INTRODUCTION

Since the pioneering work of Haldane [1], there has been great interest in the topological properties of materials systems, with many exciting developments in the past dozen years [2–4]. However, much of the progress on topological systems has been focused on topological classes with time-reversal symmetry (TRS), and topological materials with broken TRS, i.e., magnetic materials, remain challenging to design and study. The zero-field quantum anomalous Hall effect in particular has been realized only in magnetically doped topological insulators, with sub-Kelvin temperatures necessary to observe robust quantization, limiting possible applications of this effect [5–8].

MnBi_2Te_4 and MnBi_2Se_4 have recently been the subject of intensive study [9–23], due to theoretical predictions [24–30] that they are antiferromagnetic (AFM) topological insulators (TI), a type of axion insulator, in bulk [31–34]. In addition, they can display Weyl semimetal phases under strain and/or external magnetic field. In 2D geometries, they are predicted to be Chern insulators for systems with an odd number of layers. This materials class offers the possibility of observing broken-TRS topological effects in single-crystal materials with reasonably high magnetic transition temperatures ($T_N \approx 24$ K [26]) and large band gaps, which should improve the robustness of the topological effects. However, there has been some disagreement between experiments and theoretical expectations, and in some cases between different experiments, on fundamental properties of this material. Under external magnetic field sufficient to drive a transition from the layered AFM ground state to a fully spin-polarized ferromagnetic (FM) state, the quantum anomalous Hall effect has been observed, as expected, but the anomalous Hall conductivity (AHC) of odd-layer systems is not observed to be quantized

at zero field [11,12]. In addition, several experiments have observed surface state features even below the Néel temperature [14–18,26,35,36], which are expected to be gapped by the broken TRS on the surface, while other experiments have seen inconsistent or conflicting results [6,13,14,19,37] (see discussion in Ref. [18]). Either a different surface magnetic ordering or domain walls [15–18] have been suggested as possible explanations for the low-temperature surface states. Recently the presence of domain walls has been confirmed using atomic-force microscopy [38], but at relatively low densities, while robust surface A-type AFM ordering has also been confirmed [36,39].

To address these discrepancies, in this work, we develop a first principles-based model of the magnetic degrees of freedom and electronic structure of MnBi_2Te_4 that can be applied to large unit-cells. Using this model, we can directly calculate some of the proposed scenarios for explaining the various experimental results, which may help clarify the experimental situation. We first briefly consider the isosymmetric topological transition that occurs as a function of spin-orbit coupling (SOC) strength. Next, we study the temperature-driven topological phase transition that accompanies the Néel transition, observing how the bulk and surface band structures change in response to changes in the spin ordering. We find that consistent with expectations, the system has a bulk band gap both above and below the transition temperature, but has a surface state above T_N only when TRS is restored. We also consider configurations with partially ordered surface spins, and we find that such configurations can cause the surface gap to close if the disorder is large enough, even if the surface still has broken TRS on average. Finally, we study domain walls in low-temperature MnBi_2Te_4 , which can be understood as a type of topological transition that occurs as a function of spatial location [26,31,40]. We find spin-polarized metallic edge states localized on the surface at the domain walls but that extend over many unit-cells along the surface perpendicular to the domain wall. These surface features can appear similar

^{*}kevin.garrity@nist.gov

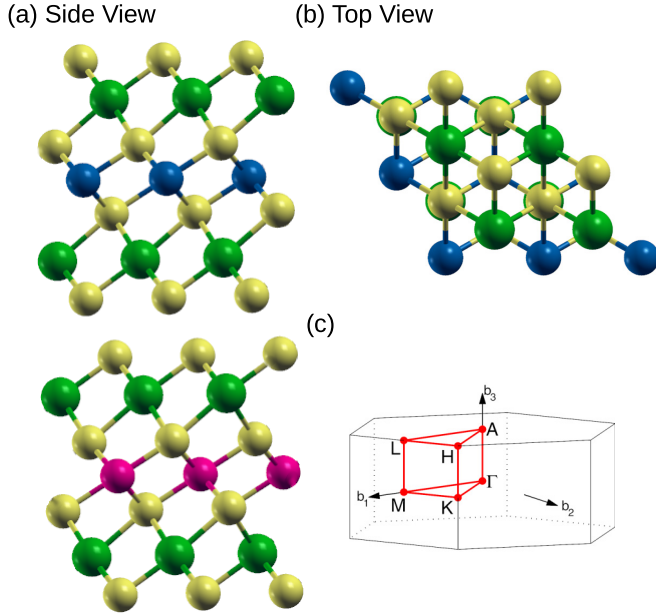


FIG. 1. (a)–(b) Side and top views of layered AFM structure of MnBi₂Te₄. Mn spin up is red and spin down is blue, Te is yellow, and Bi is green. (c) Brillouin zone. We use hexagonal labels to more easily compare bulk and surface calculations.

to the topological surface states we observe in the disordered spin configurations, which may help reconcile some of the unexpected experimental observations with theory.

We show the crystal structure of MnBi₂Te₄, space group $R\bar{3}m$, in Fig. 1. The structure consists of a stack of seven atom layers (septuple layers). In the ground state, the Mn within each layer are ordered ferromagnetically, and alternating layers are aligned antiferromagnetically, with spins oriented along the $\pm z$ direction.

II. METHODS

A. First principles

We perform first principles density functional theory (DFT) calculations [41,42] with the Quantum Espresso code [43] using the PBEsol [44] functional. We use a DFT + U correction with $U = 3$ eV on the Mn- d states [45–47]. We use norm-conserving ONCV pseudopotentials with SOC [48–50]. We use Wannier90 [51–53] to generate first-principles tight-binding Hamiltonians, and we calculate topological invariants with both WannierTools [54] and our own code. Our initial Wannier projection consists of Bi/Te- p orbitals and Mn- d orbitals, which describes all the bands near the Fermi level.

B. Magnetic tight-binding model

In order to calculate the electronic structure of the large unit-cells that are necessary to treat structures with disordered spins or domain walls, we develop a tight-binding model, based on Wannier Hamiltonians, that allows us to calculate the electronic structure for arbitrary orientations of the Mn spins, as well as variable SOC. The model is similar in spirit to the model in Ref. [55], which treats chemical disorder in topological insulators. The basis of our model is three separate

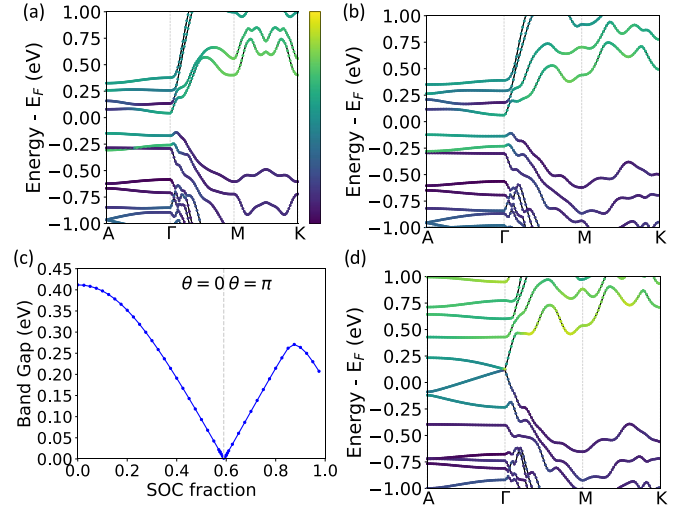


FIG. 2. (a) Band structure of AFM phase with spins in z -direction calculated using DFT. (b) The same but calculated with model. The colors show projections onto Bi Wannier functions. (c) Band gap in eV as a function of SOC fraction. (d) Model band structure at SOC = 0.59, the critical value.

DFT plus Wannier calculations. First, we perform a calculation with TRS and without SOC, getting the Hamiltonian H^{TRS} . Second, we perform a calculation with TRS and SOC, getting $H_{\text{SOC}}^{\text{TRS}}$. By subtracting these two Hamiltonians, we can isolate the SOC contribution, $H_{\text{SOC}} = H_{\text{SOC}}^{\text{TRS}} - H^{\text{TRS}}$. Finally, we perform a FM calculation without SOC, which is separated into independent spin up (H^{up}) and spin down (H^{dn}) terms.

We then assemble the total model for a single unit-cell, H_{tot} :

$$H_{\text{avg}} = \frac{1}{2}(H^{\text{up}} + H^{\text{dn}}), \quad (1)$$

$$H_{\text{diff}} = \frac{1}{2}(H^{\text{up}} - H^{\text{dn}}), \quad (2)$$

$$H_{\text{tot}} = H_{\text{avg}}\sigma_0 + H_{\text{diff}}(\mathbf{m} \cdot \boldsymbol{\sigma}) + H_{\text{SOC}}, \quad (3)$$

where the vector \mathbf{m} is the normalized magnetization direction, σ_0 is the identity matrix, and $\boldsymbol{\sigma}$ are the three Pauli matrices. To generate tight-binding Hamiltonians for supercells with different magnetic orderings (\mathbf{m} 's) in each cell, we keep the onsite terms as above and average the intercell matrix elements. This approximation allows us to treat arbitrary magnetic orderings based solely on FM DFT calculations, and we verify its accuracy below.

To construct surfaces, we create supercells of the desired thickness but then set to zero any hoppings that would go across the surface. This approximation is reasonable for MnBi₂Te₄ because of the layered crystal structure, and direct surface calculations show that the surface relaxation energy of MnBi₂Te₄ is only 5 meV per surface unit-cell. We can also artificially adjust the magnitude of the SOC by multiplying the final term in the model by a number between zero and one.

In order to verify the accuracy of this model, we compare the model band structure to equivalent calculations done directly with DFT-derived Wannier Hamiltonians for several spin configurations. In Figs. 2(a) and 2(b) we show the DFT and model band structures for the ground state AFM phase

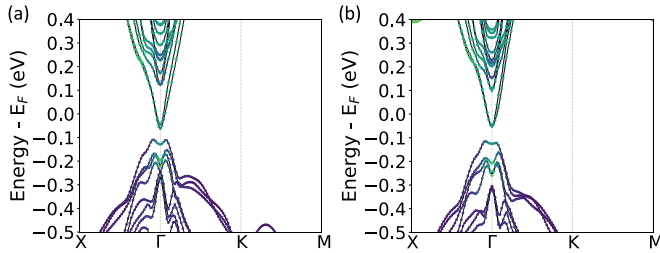


FIG. 3. (a) DFT and (b) model band structure of three layer slab with surfaces, with out-of-plane AFM spin ordering. The DFT calculation includes surface relaxation. Colors as in Fig. 2.

with spins in the $\pm z$ -direction. Comparing the two figures, we find excellent agreement, with all major features of the band structure reproduced by the model. We emphasize that the model is built using only FM spin configurations and only nonmagnetic SOC calculations, so its success describing an AFM calculation with SOC is encouraging. We show several more bulk band structure comparisons with various spin orderings in Fig. S1 of the Supplemental Materials [56]. In Fig. 3 we directly compare a three-layer-thick surface DFT calculation with our model. For both the bulk and surface calculations, we find excellent agreement. In order to interpret the band structures of systems with large unit-cells and magnetic disorder, we use band unfolding to produce effective primitive cell spectral functions [55,57–59].

C. Spin model

Similar to previous works on this material class [24,26], we model the energetics of the spin-spin interactions in our system using a Heisenberg model with onsite anisotropy:

$$H = \frac{1}{2} \sum_{ij} J_{ij} \vec{S}_i \cdot \vec{S}_j + \sum_i A |S_i^z|^2. \quad (4)$$

We treat the \vec{S}_i variables as classic spins. We fit the coupling parameters, J_{ij} and A , using a least squares approach and taking into account crystal symmetries [60]. Symmetry allows for additional anisotropic intersite coupling terms in magnetic materials with spin-orbit coupling; however, given the success of the previous works [26] describing magnetic interactions in MnBi_2Te_4 , we limit our model to Heisenberg intersite terms. We fit to DFT calculations of various spin configurations in the equivalent of $2 \times 2 \times 2$ and $3 \times 3 \times 3$ unit-cells, using the method of Lloyd-Williams *et al.* to generate smaller nondiagonal cells [61]. We then use Metropolis Monte Carlo sampling to generate spin configurations at a given temperature [62].

III. RESULTS

A. Variable spin-orbit

Using our tight-binding model, we can now study changes in the electronic structure during several types of topological phase transitions. As a warm-up, we first consider the isosymmetric topological transition that occurs when artificially varying the strength of the SOC. In Fig. 2(c) we show the band gap of the ground state AFM phase as a function of the strength of SOC. The nontrivial AFM topological state of

MnBi_2Te_4 is driven by SOC-induced band inversion. Therefore, at zero SOC, MnBi_2Te_4 is a trivial AFM insulator. As the fraction of SOC is increased, the bulk band gap closes, and at the critical value of the SOC, 0.59, the band structure becomes inverted. Above this value, our model is in a topologically nontrivial AFM insulating phase, which is also an axion insulator. This transition is an example of an isosymmetric transition between a topologically nontrivial and trivial state, which requires a bulk gap closure. In practice, directly controlling the SOC experimentally is not possible, but this transition might be similar to a topological transition that occurs as a function of doping elements with weaker SOC into the MnBi_2Te_4 structure.

B. Temperature-dependent electronic structure

Next, we consider the topological phase transition that occurs as a function of temperature. Above the Néel temperature, the spins in MnBi_2Te_4 become disordered, restoring TRS on average and causing a topological phase transition.

We generate spin configurations at a given temperature using our magnetic model (see Sec. II C). We find that our model has a transition temperature of 40 K, which is in reasonable agreement with experiment, considering that quantum fluctuations lower transition temperatures. As expected for a layered structure, we find that within-layer spin-spin correlations are much larger than interlayer correlations and remain small but nonzero above the transition temperature (see Figs. S2 and S3 [56] for more details).

Using our magnetic model, we can generate spin configurations at a given temperature, and then study the average electronic structure using our tight-binding model. We first perform this analysis in a periodic $3 \times 3 \times 6$ unit-cell without a surface. We confirm that the bulk gap does not close near T_N , which is consistent with the fact that the bands near the Fermi level are primarily Bi and Te states, with the Mn supplying spin-splitting. In fact, the bulk gap opens slightly, as shown by the dashed line in Fig. 4(a) (see also Fig. S5 and S6 [56]). Unlike the isosymmetric SOC-driven transition studied above, here, the order-to-disorder spin transition restores TRS at high temperatures. Because of the symmetry change, the relevant topological invariants are different above and below T_N , and no bulk gap closure is required despite the topological transition.

Next, we monitor the same transition, but in $3 \times 3 \times 5$ unit-cell, with surfaces perpendicular to the z -direction. In this odd-layered case, we find that MnBi_2Te_4 is a Chern insulator at zero temperature, consistent with previous work [24–26]. In Fig. 4(a) the blue points are the gaps of individual spin configurations, and the solid red line shows the minimum gap at each temperature. We find that above T_N , the minimum surface gap closes. Individual spin configurations can have small gaps of ≈ 25 meV even above T_N , which we attribute to spin fluctuations breaking TRS. We expect that unit-cells with larger areas than we can easily calculate would have smaller minimum gap fluctuations above T_N , but that a spatially local measurement of the gap would continue to fluctuate.

In Figs. 4(b)–4(d), we show the unfolded surface band structure, averaged over 20 spin configurations, at $T = 1$ K, 25 K, and 100 K, respectively. At low temperature, when the

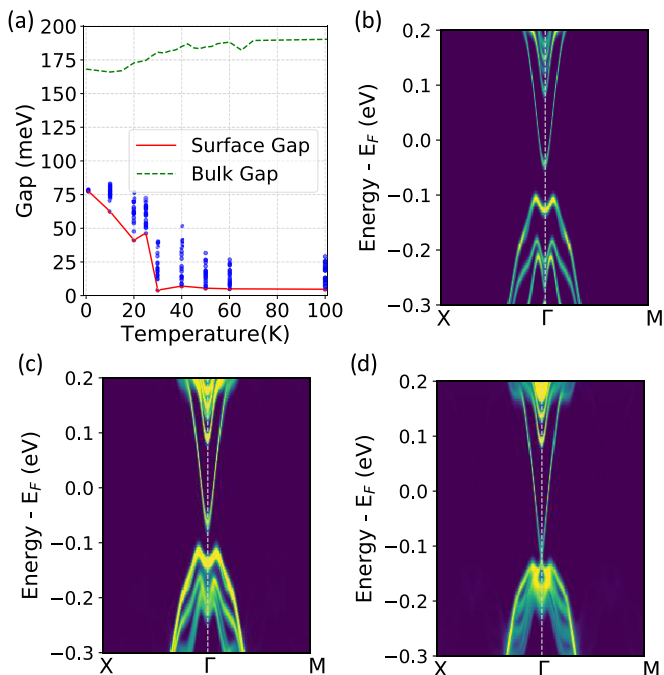


FIG. 4. (a) Band gap (meV) versus temperature. Solid red line: minimum surface gap. Dashed green line: mean bulk gap. Blue points: individual surface calculations. (b)–(d) Unfolded average surface band structure at 1 K, 25 K, and 100 K, respectively.

spins are almost perfectly aligned, we find sharply defined bands and a clear band gap. However, as the temperature is raised to 25 K, which is slightly below the Néel temperature in our model, the bands become more diffuse, and the spin-polarized bands begin to show the influence of disorder. In addition, the gap at Γ begins to close. Finally, at 100 K, we find a closed gap, with a clear Dirac cone surface feature, which shows that the system is in a nontrivial TRS-invariant ($Z_2 = 1$) topological insulating state. This average topological state emerges despite the fact that the individual band structures that go into the average break TRS.

C. Surface spin disorder

To better quantify the amount of disorder necessary to close the surface band gap, we again consider a $3 \times 3 \times 5$ supercell with surfaces, but now we keep the bulk three layers fixed to a perfectly ordered AFM configuration and consider partially disordered surface spins. Specifically, we choose surface spins such that each spin is a mixture of a perfectly ordered spin, oriented along the z direction, and a randomly oriented spin. We consider a range of mixing fractions from 0 (perfectly ordered surface) to 1 (fully disordered). Notably, all of the surface spin configurations with disorder fraction < 1 have broken TRS on the surface on average. Despite this broken TRS, we find that disorder fractions above 0.5 are enough to close the average surface gap, as shown in Figs. 5(a) and 5(b). As discussed above, thermal fluctuations alone are not enough to close the surface band gap at temperatures significantly below T_N . Other possible sources of spin disorder include quantum spin fluctuations or chemical disorder.

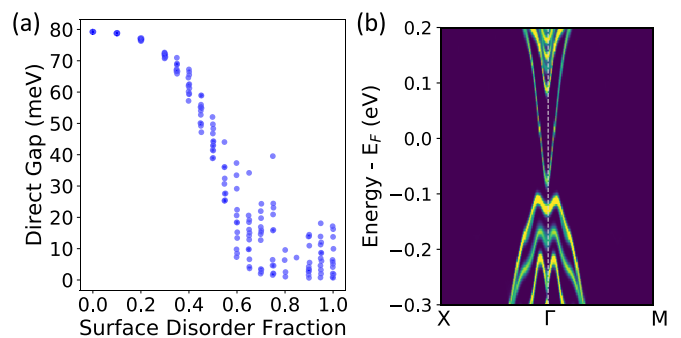


FIG. 5. (a) Surface band gap (meV) of $3 \times 3 \times 5$ supercell with ordered bulk and partially disordered surface spins. Each point is one spin configuration. (b) Unfolded averaged band structure at 0.5 mixing between ordered and disordered surface spins.

D. Domain wall electronic structure

The above discussion of temperature-driven topological states provides a clear explanation of the surface features observed experimentally above T_N ; however, the states observed at low temperature remain unexplained. One possible explanation is that the low-temperature surface spin configuration does not match the theoretical predictions. However, in this section, we consider the alternate explanation that there is a significant density of domains in the AFM phase at low temperature, possibly pinned by sample-dependent defects. In the bulk of an AFM topological insulator, the topological index on either side of a domain boundary is the same, as the spin configurations are related by a translation by one layer in the z -direction. Therefore, a gap closure at the domain wall is not required. Equivalently, the axion angle of both domains equals $\pi \pm 2\pi$ [31,34]. However, in the presence of a surface, this translation is no longer possible. Each surface of an AFM TI contributes $\pm \frac{e^2}{2h}$ to the total AHC, with the sign determined by the direction of the spins in the top layer [31]. Therefore, there are two distinct topological phases at the surface of an AFM TI, and a domain wall between these surfaces must have a 1D conducting channel that contributes a total of $\pm \frac{e^2}{h}$ to the AHC. In this work, we consider sharp Ising-like domain walls, where the spins suddenly change from $+z$ to $-z$, or vice versa, at the boundary. Of course, more complicated configurations where the spins rotate gradually (Bloch-like) are also possible; however, we will find that even sharp interfaces result in extended conducting states. Furthermore, we note that similar considerations apply to step edges.

Using our model, we first study domains in a $24 \times 1 \times 5$ unit cell, with surfaces in the z direction, with two domains 12 unit cells wide, and therefore two domain walls. As expected, we find a gap closure at $k = \Gamma$, with four degenerate states. These states correspond to the states localized at the two domain walls on each surface, although at the degeneracy point they are all mixed together. To make the plotting clearer, we move slightly away from Γ , and consider two empty degenerate states at $k_x = 0.05 \frac{2\pi}{a}$. In Fig. 6(a) we plot $|\psi|^2$ for that pair of states, using larger circles to represent larger magnitudes of the eigenvector. We find that, as expected, the pair of eigenvectors are surface states localized at the domain walls at $x = 0$ and $x = 0.5$ on the bottom and top surfaces. Even though we fix the spins to reverse direction abruptly

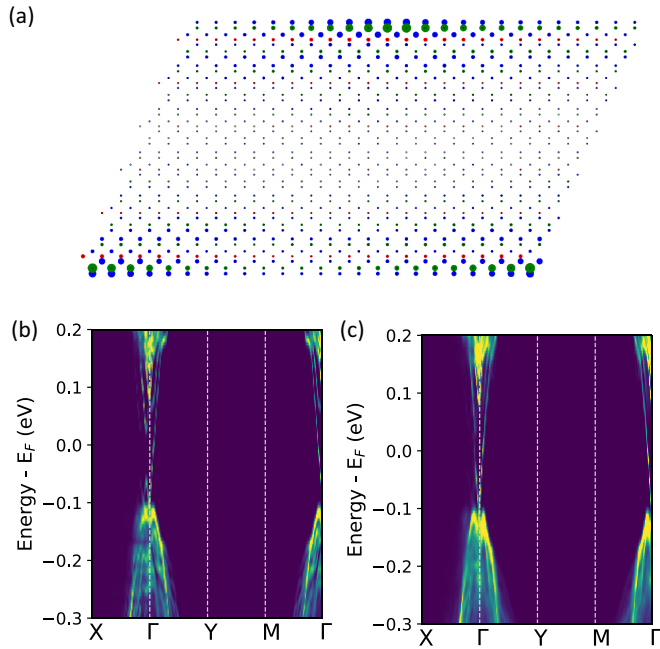


FIG. 6. (a) Real-space representation of $|\psi|^2$ localized at domain wall in $24 \times 1 \times 5$ cell. Larger circles have more weight. Blue circles are Te, green are Bi, and red are Mn. (b) Unfolded band structure in $20 \times 1 \times 5$ unit-cell with 10 unit-cell domains. (c) Average unfolded band structure.

at the domain wall, we see that the electronic states decay rather slowly perpendicular to the domain wall, extending ≈ 10 unit-cells around the wall.

In Fig. 6(b) we consider the unfolded band structure for a single example of a pair of domains, in a $20 \times 1 \times 5$ unit cell. We see that there is a gap closure at Γ , and that the band structure looks somewhat similar to the 2D topological surface state for disordered spins [see Fig. 4(d)], even though the metallic edge channel is 1D. However, because we are only considering a single pair of perfectly ordered and periodic domains, the unfolded topological surface band has a variety of artifacts related to wave vectors of the superlattice. In an experimental situation, we expect that there will instead be domains of varying sizes. Therefore, in Fig. 6(c) we average the unfolded surface band structures of dozens of similar domains, with thicknesses of 4 to 10 unit cells, in supercells of 8 to 20 unit-cells. We see that we recover an average band

structure that looks quite similar to the 2D topological surface state with disordered spins shown in Fig. 4(d), even though every spin is perfectly aligned along the $\pm z$ direction and the domain walls are sharp and aligned. We expect that if we go even further and include configurations with partially disordered spins and domain walls in varying directions, the result will be band structures that closely resemble the Dirac cone features we see at high temperatures.

IV. CONCLUSIONS

In conclusion, we generated a model to study the electronic structure of large unit-cells of the AFM topological insulator MnBi_2Te_4 with arbitrary spin configurations, which we have used to study three types of topological phase transitions. First, we considered an artificial transition driven by adjusting the magnitude of the SOC, which proceeds via a bulk gap closure. Next, we considered a topological transition driven by a temperature-dependent magnetic ordering. We find that as TRS is restored on average above T_N , MnBi_2Te_4 goes from an AFM topological insulator with a surface gap to a TRS-invariant Z_2 topological insulator with an associated Dirac cone surface state, but with minimal change in the bulk gap. Finally, we consider the electronic surface states associated with AFM domain walls, which are 1D topological states. We find that these states are strongly localized at the surface, but extend many unit-cells perpendicular to the domain walls, and that many 1D domain walls can together resemble a Dirac cone-like topological surface state on average.

Consistent with previous ideas, this work suggests that additional sources of spin disorder beyond thermal fluctuations are necessary to explain the gapless states observed experimentally at low temperatures. We address this possibility more quantitatively, finding that partially ordered surface spin configurations with broken TRS can still result in a closed surface band gap. However, disorder fractions above 50% are necessary to fully close the surface gap. Possible sources of disorder beyond thermal fluctuations include quantum fluctuations or chemical disorder. Alternatively, AFM domain walls can produce electronic features that mimic the closed band gap seen above T_N . Further experiments that quantify the local band gap of MnBi_2Te_4 and that correlate the local gap with ARPES and transport experiments may help clarify the topology and electronic structure in this material.

- [1] F. D. M. Haldane, *Phys. Rev. Lett.* **61**, 2015 (1988).
- [2] M. Z. Hasan and C. L. Kane, *Rev. Mod. Phys.* **82**, 3045 (2010).
- [3] X.-L. Qi and S.-C. Zhang, *Rev. Mod. Phys.* **83**, 1057 (2011).
- [4] Y. Tokura, K. Yasuda, and A. Tsukazaki, *Nat. Rev. Phys.* **1**, 126 (2019).
- [5] Y. Chen, J.-H. Chu, J. Analytis, Z. Liu, K. Igarashi, H.-H. Kuo, X. Qi, S.-K. Mo, R. Moore, D. Lu *et al.*, *Science* **329**, 659 (2010).
- [6] C.-Z. Chang, J. Zhang, X. Feng, J. Shen, Z. Zhang, M. Guo, K. Li, Y. Ou, P. Wei, L.-L. Wang *et al.*, *Science* **340**, 167 (2013).
- [7] C.-Z. Chang, W. Zhao, D. Y. Kim, H. Zhang, B. A. Assaf, D. Heiman, S.-C. Zhang, C. Liu, M. H. Chan, and J. S. Moodera, *Nat. Mater.* **14**, 473 (2015).
- [8] I. Lee, C. K. Kim, J. Lee, S. J. Billinge, R. Zhong, J. A. Schneeloch, T. Liu, T. Valla, J. M. Tranquada, G. Gu *et al.*, *Proc. Natl. Acad. Sci. USA* **112**, 1316 (2015).
- [9] D. S. Lee, T.-H. Kim, C.-H. Park, C.-Y. Chung, Y. S. Lim, W.-S. Seo, and H.-H. Park, *CrystEngComm* **15**, 5532 (2013).
- [10] J. A. Hagmann, X. Li, S. Chowdhury, S.-N. Dong, S. Rouvimov, S. J. Pookpanratana, K. M. Yu, T. A. Orlova, T. B. Bolin, C. U. Segre *et al.*, *New J. Phys.* **19**, 085002 (2017).
- [11] Y. Deng, Y. Yu, M. Z. Shi, Z. Guo, Z. Xu, J. Wang, X. H. Chen, and Y. Zhang, *Science* **367**, 895 (2020).
- [12] C. Liu, Y. Wang, H. Li, Y. Wu, Y. Li, J. Li, K. He, Y. Xu, J. Zhang, and Y. Wang, *Nat. Mater.* **19**, 522 (2020).

- [13] B. Chen, F. Fei, D. Zhang, B. Zhang, W. Liu, S. Zhang, P. Wang, B. Wei, Y. Zhang, Z. Zuo *et al.*, *Nat. Commun.* **10**, 4469 (2019).
- [14] R. C. Vidal, H. Bentmann, T. R. F. Peixoto, A. Zeugner, S. Moser, C.-H. Min, S. Schatz, K. Kißner, M. Ünzelmann, C. I. Fornari *et al.*, *Phys. Rev. B* **100**, 121104(R) (2019).
- [15] P. Swatek, Y. Wu, L.-L. Wang, K. Lee, B. Schrunk, J. Yan, and A. Kaminski, Gapless dirac surface states in the antiferromagnetic topological insulator MnBi_2Te_4 , *Phys. Rev. B* **101**, 161109 (2020).
- [16] H. Li, S.-Y. Gao, S.-F. Duan, Y.-F. Xu, K.-J. Zhu, S.-J. Tian, J.-C. Gao, W.-H. Fan, Z.-C. Rao, J.-R. Huang *et al.*, *Phys. Rev. X* **9**, 041039 (2019).
- [17] Y.-J. Hao, P. Liu, Y. Feng, X.-M. Ma, E. F. Schwier, M. Arita, S. Kumar, C. Hu, R. Lu, M. Zeng *et al.*, *Phys. Rev. X* **9**, 041038 (2019).
- [18] Y. J. Chen, L. X. Xu, J. H. Li, Y. W. Li, H. Y. Wang, C. F. Zhang, H. Li, Y. Wu, A. J. Liang, C. Chen *et al.*, *Phys. Rev. X* **9**, 041040 (2019).
- [19] S. H. Lee, Y. Zhu, Y. Wang, L. Miao, T. Pillsbury, H. Yi, S. Kempinger, J. Hu, C. A. Heikes, P. Quarterman *et al.*, *Phys. Rev. Res.* **1**, 012011 (2019).
- [20] D. Xiao, J. Jiang, J.-H. Shin, W. Wang, F. Wang, Y.-F. Zhao, C. Liu, W. Wu, M. H. Chan, N. Samarth, and C.Z. Chang, *Phys. Rev. Lett.* **120**, 056801 (2018).
- [21] J. Li, Y. Li, S. Du, Z. Wang, B.-L. Gu, S.-C. Zhang, K. He, W. Duan, and Y. Xu, *Sci. Adv.* **5**, eaaw5685 (2019).
- [22] Y. Gong, J. Guo, J. Li, K. Zhu, M. Liao, X. Liu, Q. Zhang, L. Gu, L. Tang, X. Feng *et al.*, *Chin. Phys. Lett.* **36**, 076801 (2019).
- [23] E. D. L. Rienks, S. Wimmer, J. Sánchez-Barriga, O. Caha, P. S. Mandal, J. Ruzicka, A. Ney, H. Steiner, V. V. Volobuev, H. Groiss *et al.*, *Nature (London)* **576**, 423 (2019).
- [24] S. Chowdhury, K. F. Garrity, and F. Tavazza, *npj Comput. Mater.* **5**, 33 (2019).
- [25] D. Zhang, M. Shi, T. Zhu, D. Xing, H. Zhang, and J. Wang, *Phys. Rev. Lett.* **122**, 206401 (2019).
- [26] M. M. Otrokov, I. I. Klimovskikh, H. Bentmann, D. Estyunin, A. Zeugner, Z. S. Aliev, S. Gaß, A. U. B. Wolter, A. V. Koroleva, A. M. Shikin *et al.*, *Nature (London)* **576**, 416 (2019).
- [27] S. V. Eremeev, M. M. Otrokov, and E. V. Chulkov, *Nano Lett.* **18**, 6521 (2018).
- [28] M. Otrokov, T. V. Menshchikova, I. Rusinov, M. Vergniory, V. M. Kuznetsov, and E. V. Chulkov, *JETP Lett.* **105**, 297 (2017).
- [29] M. M. Otrokov, T. V. Menshchikova, M. G. Vergniory, I. P. Rusinov, A. Y. Vyazovskaya, Y. M. Koroteev, G. Bihlmayer, A. Ernst, P. M. Echenique, A. Arnau *et al.*, *2D Materials* **4**, 025082 (2017).
- [30] R.-X. Zhang, F. Wu, and S. Das Sarma, *Phys. Rev. Lett.* **124**, 136407 (2020).
- [31] R. S. K. Mong, A. M. Essin, and J. E. Moore, *Phys. Rev. B* **81**, 245209 (2010).
- [32] R. Li, J. Wang, X.-L. Qi, and S.-C. Zhang, *Nat. Phys.* **6**, 284 (2010).
- [33] J. Wang, B. Lian, and S.-C. Zhang, *Phys. Rev. B* **93**, 045115 (2016).
- [34] A. M. Essin, J. E. Moore, and D. Vanderbilt, *Phys. Rev. Lett.* **102**, 146805 (2009).
- [35] R. C. Vidal, A. Zeugner, J. I. Facio, R. Ray, M. H. Haghghi, A. U. Wolter, L. T. C. Bohorquez, F. Cagliaris, S. Moser, T. Figgemeier *et al.*, *Phys. Rev. X* **9**, 041065 (2019).
- [36] D. Nevola, H. X. Li, J.-Q. Yan, R. G. Moore, H.-N. Lee, H. Miao, and P. D. Johnson, *Phys. Rev. Lett.* **125**, 117205 (2020).
- [37] A. Zeugner, F. Nietschke, A. U. Wolter, S. Gaß, R. C. Vidal, T. R. Peixoto, D. Pohl, C. Damm, A. Lubk, R. Hentrich *et al.*, *Chem. Mater.* **31**, 2795 (2019).
- [38] P. M. Sass, W. Ge, J. Yan, D. Obeysekera, J. J. Yang, and W. Wu, *Nano Lett.* **20**, 2609 (2020).
- [39] P. M. Sass, J. Kim, D. Vanderbilt, J. Yan, and W. Wu, *Phys. Rev. Lett.* **125**, 037201 (2020).
- [40] J. Zhang, Z. Liu, and J. Wang, *Phys. Rev. B* **100**, 165117 (2019).
- [41] P. Hohenberg and W. Kohn, *Phys. Rev.* **136**, B864 (1964).
- [42] W. Kohn and L. Sham, *Phys. Rev.* **140**, A1133 (1965).
- [43] P. Giannozzi, S. Baroni, N. Bonini, M. Calandra, R. Car, C. Cavazzoni, D. Ceresoli, G.L. Chiarotti, M. Cococcioni, I. Dabo *et al.*, *J. Phys.: Condens. Matter* **21**, 395502 (2009).
- [44] J. P. Perdew, A. Ruzsinszky, G. I. Csonka, O. A. Vydrov, G. E. Scuseria, L. A. Constantin, X. Zhou, and K. Burke, *Phys. Rev. Lett.* **100**, 136406 (2008).
- [45] V. I. Anisimov, J. Zaanen, and O. K. Andersen, *Phys. Rev. B* **44**, 943 (1991).
- [46] S. L. Dudarev, G. A. Botton, S. Y. Savrasov, C. J. Humphreys, and A. P. Sutton, *Phys. Rev. B* **57**, 1505 (1998).
- [47] V. Stevanović, S. Lany, X. Zhang, and A. Zunger, *Phys. Rev. B* **85**, 115104 (2012).
- [48] D. R. Hamann, *Phys. Rev. B* **88**, 085117 (2013).
- [49] M. Schlipf and F. Gygi, *Comput. Phys. Commun.* **196**, 36 (2015).
- [50] P. Scherpelz, M. Govoni, I. Hamada, and G. Galli, *J. Chem. Theory Comput.* **12**, 3523 (2016).
- [51] A. A. Mostofi, J. R. Yates, Y.-S. Lee, I. Souza, D. Vanderbilt, and N. Marzari, *Comput. Phys. Commun.* **178**, 685 (2008).
- [52] I. Souza, N. Marzari, and D. Vanderbilt, *Phys. Rev. B* **65**, 035109 (2001).
- [53] N. Marzari and D. Vanderbilt, *Phys. Rev. B* **56**, 12847 (1997).
- [54] Q. Wu, S. Zhang, H.-F. Song, M. Troyer, and A. A. Soluyanov, *Comput. Phys. Commun.* **224**, 405 (2018).
- [55] J. Liu and D. Vanderbilt, *Phys. Rev. B* **88**, 224202 (2013).
- [56] See Supplemental Material at <http://link.aps.org/supplemental/10.1103/PhysRevMaterials.5.024207> for details of the tight-binding and magnetic models.
- [57] W. Ku, T. Berlijn, C.-C. Lee *et al.*, *Phys. Rev. Lett.* **104**, 216401 (2010).
- [58] T. Berlijn, D. Volja, and W. Ku, *Phys. Rev. Lett.* **106**, 077005 (2011).
- [59] V. Popescu and A. Zunger, *Phys. Rev. Lett.* **104**, 236403 (2010).
- [60] K. F. Garrity, *Phys. Rev. B* **99**, 174108 (2019).
- [61] J. H. Lloyd-Williams and B. Monserrat, *Phys. Rev. B* **92**, 184301 (2015).
- [62] W. K. Hastings, *Biometrika* **57**, 97 (1970).